Journal of
Applied Remote Sensing

RemoteSensing.SPIEDigitalLibrary.org

Hyperspectral imaging of minerals in the longwave infrared: the use of laboratory directional-hemispherical reference measurements for field exploration data

Tanya L. Myers
Timothy J. Johnson
Neal B. Gallagher
Bruce E. Bernacki
Toya N. Beiswenger
James E. Szecsody
Russell G. Tonkyn
Ashley M. Bradley
Yin-Fong Su
Tyler O. Danby

Tanya L. Myers, Timothy J. Johnson, Neal B. Gallagher, Bruce E. Bernacki, Toya N. Beiswenger, James E. Szecsody, Russell G. Tonkyn, Ashley M. Bradley, Yin-Fong Su, Tyler O. Danby, "Hyperspectral imaging of minerals in the longwave infrared: the use of laboratory directional-hemispherical reference measurements for field exploration data," *J. Appl. Remote Sens.* **13**(3), 034527 (2019), doi: 10.1117/1.JRS.13.034527.

SPIE.

Hyperspectral imaging of minerals in the longwave infrared: the use of laboratory directional-hemispherical reference measurements for field exploration data

Tanya L. Myers,[a],* Timothy J. Johnson,[a] Neal B. Gallagher,[b] Bruce E. Bernacki,[a] Toya N. Beiswenger,[a] James E. Szecsody,[a] Russell G. Tonkyn,[a] Ashley M. Bradley,[a] Yin-Fong Su,[a] and Tyler O. Danby[a]

[a]Pacific Northwest National Laboratory, Richland, Washington, United States
[b]Eigenvector Research, Inc., Manson, Washington, United States

Abstract. Hyperspectral imaging (HSI) continues to grow as a method for remote detection of vegetation, materials, minerals, and pure chemicals. We have used a longwave infrared (7.7 to 11.8 μm) imaging spectrometer in a static outdoor experiment to collect HSI data from 24 minerals and background materials to determine the efficacy with which HSI can remotely detect and distinguish both pure minerals and mineral mixtures at a 45-deg tilt angle relative to ground using two different backgrounds. Measurements were obtained separately for the minerals and materials mounted directly on both a bare plywood board and a board coated with aluminum foil: 19 powders (3 mixtures and 16 pure mineral powders) held in polyethylene bottle lids as well as five samples in rock form were taped directly to the boards. The primary goal of the experiment was to demonstrate that a longwave infrared library of solids and minerals collected as directional-hemispherical reflectance spectra in the laboratory could be used directly for HSI field identification along with simple algorithms for a rapid survey of the target materials. Prior to the experiment, all 24 mineral/inorganic samples were measured in the laboratory using a Fourier transform infrared spectrometer equipped with a gold-coated integrating sphere; the spectra were assimilated as part of a larger reference library of 21 pure minerals, 3 mixtures, and the polyethylene lid. Principal component analysis with mean-centering was used in an exploratory analysis of the HSI images and showed that, for the aluminum-coated board, the first principal component captured the difference between the signal that resembled a blackbody and the highly reflective aluminum background. In contrast, the second, third, and fourth principal components were able to discriminate the materials including phosphates, silicates, carbonates, and the mixtures. Results from generalized least squares target detection clearly showed that laboratory reference spectra of minerals could be utilized as targets with high fidelity for field detection. © *The Authors. Published by SPIE under a Creative Commons Attribution 4.0 Unported License. Distribution or reproduction of this work in whole or in part requires full attribution of the original publication, including its DOI.* [DOI: 10.1117/1.JRS.13.034527]

Keywords: hyperspectral imaging; longwave infrared; minerals; principal component analysis; directional hemispherical reflectance; infrared; particle size.

Paper 190301 received Apr. 19, 2019; accepted for publication Aug. 30, 2019; published online Sep. 23, 2019.

1 Introduction

In the last few decades, hyperspectral imaging (HSI) has evolved as a method for remote detection with many applications, including identification of plants, earthen materials, and natural events, such as fire or volcanic eruption.[1–3] Typically, the spectral data within an individual pixel are exploited by comparing the reflected/emitted energy of the target substance(s) (as mitigated by intervening atmosphere) with those materials' spectral characteristics, which are compiled in a separate spectral library.[4,5] Many materials have been studied with HSI and some even studied in multiple phases; much of the early HSI work focused on gas-phase detection[6,7] and a few

---

*Address all correspondence to Tanya Myers, E-mail: Tanya. Myers@pnnl.gov studies also reported liquid-phase detection.[8–10] More recent HSI studies, however, have focused on detection of solid materials, typically using reflected visible or near-infrared wavelengths.[11,12] The solid-phase studies have grown at an exponential pace, particularly for vegetation[13–15] as well as for rocks, minerals, and other geological specimens.[11,16–19] To support these geological studies, the ASTER spectral library database, for example, has grown to include over 2300 spectra for a wide variety of materials including minerals, rocks, vegetation, soils, and manmade materials covering the wavelength range 0.4 to 15.4 μm.[20] Thermal infrared (TIR) or longwave infrared (LWIR) sensors can measure known spectral features that correspond to the fundamental vibrational frequencies of interatomic bonds within common rock-forming minerals. Only a few of the geologically-based studies, however, have used TIR wavelengths, and these include the very early laboratory studies of Hunt and Salisbury, who showed that igneous,[17] sedimentary,[18] and metamorphic[19] species, particularly sedimentary species such as silicates and carbonates,[18] are readily detected by infrared reflectance spectroscopy. Many HSI studies followed in the 1980s and 1990s[21] including, e.g., the first TIR imaging studies by Kahle et al.[22] as well as several others. In many of these pioneering works, it was noted that minerals containing anion chemical moieties such as silicates,[23] carbonates,[24] phosphates,[25] sulfates,[26] or cations such as ammonium or uranyl[27,28] are all known to display characteristically strong emission/reflectance features in the LWIR between 7 and 13 μm, making them amenable to such TIR detection.

There are now several modalities available for HSI including handheld sensors,[29,30] field portable systems,[31] and airborne systems.[32–36] With the deployment of LWIR systems such as the spatially enhanced broadband array spectrograph system (SEBASS) hyperspectral imager,[34] the last 20 years have even seen airborne detection of rocks and minerals. For example, Aslett et al.[37] recently reported detection of rock forming minerals at Death Valley National Park in California using areal SEABASS data.

The reflectance spectra of solid materials, however, can vary significantly, especially in the LWIR,[38,39] and multiple spectra may be needed for identification of the same solid species as opposed to gases, where only a single reference spectrum is needed.[40,41] Reflectance spectra for solids depend on both real and imaginary components (n, k) of the complex refractive index as well as morphological parameters such as particle size and shape, surface roughness, etc. In the LWIR, however, the wavelength of light becomes comparable to typical solid particle sizes (e.g., 1 to 100 μm). As this happens, the measured reflectance signal becomes a more complex combination of surface scattering and volume scattering.[39,42–44] Surface scattering leads to greater reflectivity, often from reststrahlen features, where little energy has passed through grain boundaries and light scattering arises primarily from first-surface reflections.[24,44] Volume scattering, by contrast, is characterized by lower reflectivity due to inter- and intraparticle reflection, refraction, and internal absorption of the light.

It is thus understood that reflectance spectra, especially of solid materials, depend on many factors, such as sample form, grain size, and surface roughness, and are not always linear in areal coverage or concentration. The raw spectra are also a function of observational parameters such as tilt angle, temperature, and humidity and of course a function of the detector and its spectral bandwidth. To investigate some of these effects, we have conducted an HSI experiment with 24 minerals using the Telops Hyper-Cam LW, an imaging Fourier transform infrared (FTIR) spectrometer, configured to collect data in the LWIR spectral range 7.7 to 11.8 μm (1300 to 850 cm^{-1}).

In addition to investigating some of the above parameters, we wished to specifically answer the question, "Can laboratory reflectance spectra for HSI field identification along with a portable spectrometer in the LWIR be used along with relatively simple analysis to rapidly survey a set of minerals and inorganic species, including mixtures and different sample forms?" While most HSI studies employ visible or near-infrared wavelengths, we have focused on the use of laboratory mineral reflectance data for detection at infrared wavelengths, cognizant of all the grain size/sample form effects on the spectra; such effects can cause great spectral variation in the infrared (IR), especially for chemical mixtures and for mixed particle sizes.[38,39,44] We also investigated the influence of using the HSI infrared spectrometer with varying sample tilt angles (25 deg, 35 deg, and 45 deg relative to ground), as well as other temperature and diurnal effects, but those results are reported elsewhere. The primary analytical tools used for discrimination of the pure and mineral mixtures are principal component analysis (PCA) and generalized least squares (GLS) target detection as described below.

2 Experimental

Most of the minerals were obtained from commercial sources, such as Mineralogical Research Company, Wards Scientific, or Clay Mineral Society, whereas the pure chemical samples were purchased from Aldrich. Laboratory reference spectra were collected as directional-hemispherical reflectance (DHR) data using commercial FTIR spectrometers, each coupled with an integrating sphere; the experimental protocols that were followed have been detailed elsewhere.[45] The VNIR spectra were also measured, but those measurements are not discussed in this paper.[28,44]

Briefly, two types of spectra are recorded for each sample as shown in Fig. 1, namely the diffuse-only reflectance spectra and the hemispherical (a.k.a. total) reflectance, which represents the sum of the specular and diffuse components. (The hemispherical reflectance data are shown in this paper and reported as reflectance from 0 to 1.0, i.e., 0% to 100%.) For the diffuse-only measurements, a dome is removed from the upper portion of the integrating sphere[45] as shown in Fig. 1(b), allowing the specular component to escape; the dome is of the same curvature as the sphere and its size corresponds to the solid angle of the reflected IR beam. For certain species, particularly mineral specimens containing phosphates, carbonates, and silicates that can have large reststrahlen bands, the diffuse-only spectrum (i.e., without specular component) can be significantly different than the total spectrum as shown in Fig. 1 for apatite, $Ca_5(PO_4)_3(F,Cl,OH)$. The phosphate doublet band near 1100 and 1050 cm^{-1} is greatly reduced for the diffuse-only spectrum whereas only a 4% offset is observed between the hemispherical and diffuse-only spectra for most of the spectrum >1500 cm^{-1}.

Standards, including a thin polystyrene film for λ calibration, a 100% matte gold reflector, a light trap, and a calibrated diffuse hemispherical 50% reflector standard traceable to the National Institute of Standards and Technology (NIST), were measured prior to the acquisition of sample spectra to verify no major deviations in instrument performance. To check for systematic errors,

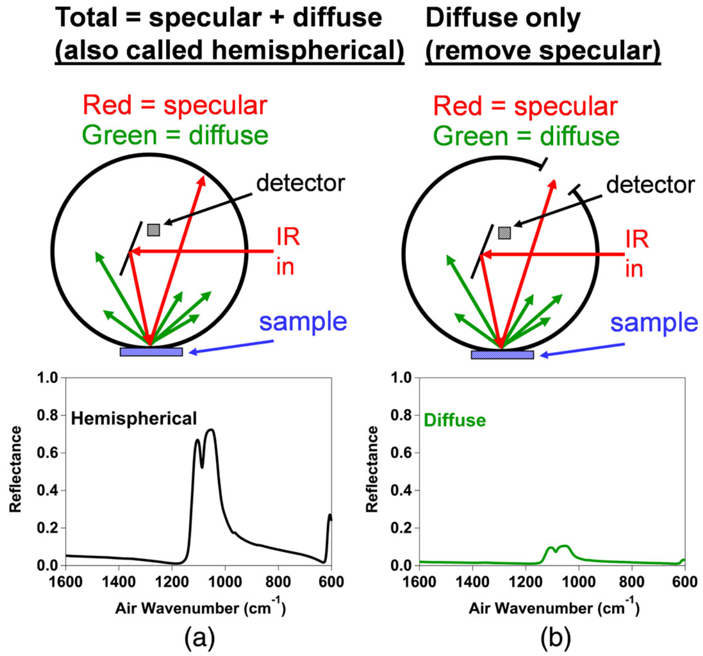

Fig. 1 Schematic of integrating sphere (top) and measured laboratory spectra of apatite in the 1600 to 600 cm^{-1} range for both (a) the total and (b) the diffuse-only spectra. For clarity, the incoming and specular rays are shown in red, arbitrary diffusely scattered light in green. For both diagrams, the flip-mirror is shown pointing down toward the sample.

multiple spectrometers were also used, and the results were compared and vetted. A Bruker IFS 66/S with an integrating sphere was used to collect DHR data for sodium carbonate, calcium carbonate, and the faux onyx samples. Spectra for the three mixtures, ammonium phosphate dibasic, sodium phosphate dibasic, and the Nalgene® lid, were recorded using a Bruker Optics IR Cube FTIR with the sphere bolted on the side as previously described.[27] A Bruker Tensor 37/A562 integrating sphere combination was used to record data for the remaining 15 samples. The spectrometer provided the modulated IR beam as input; the sphere was a Bruker A562 device, a two-port 75-mm matte-gold-coated sphere with a dedicated detector. On a vertical plane centered at the sphere's geometric center is a 2.0-cm-diameter entrance port where light from the interferometer enters the sphere. A small flip mirror near the sphere's center (Fig. 1) can rotate such that light entering the sphere can be directed downward to a 1.9-cm-diameter sample port in the bottom of the sphere, back out the entrance port, or upward to a 3.2-cm-diameter reference port that also serves as a specular exclusion port for the specular component reflected from the sample.[45–47] When the mirror is pointing down, the angle between the incident IR beam and the normal to the sample surface is 14.8 deg. The A562 sphere has a matte gold interior surface, i.e., a gold overcoat on a roughened surface, typical for such IR devices.[48] However, it has been shown[45] to display significant specular characteristics.

The sphere has a purge gas connection to provide a constant dry nitrogen purge during measurement.[46] For the mid-IR measurements reported here, the standard SiC source and Ge/KBr beamsplitter were used. The sphere's liquid nitrogen-cooled mercury cadmium telluride (MCT) detector has a 2×2 mm element with a 60-deg field of view. In combination, the system covers the 7500 to 600 cm^{-1} range. All interferograms were collected using double-sided, forward-backward acquisition at 4.0 cm^{-1} resolution, using a Mertz phase correction and Blackman-Harris 3-term apodization. Typically, 2048 scans were averaged. Key laboratory FTIR parameters are summarized in Table 1.

As described below, the HSI experiment powder samples were affixed to the boards in cups that were simply inverted lids of Nalgene® water bottles. To ensure the Nalgene (i.e., polyethylene) lids themselves would not cause an interference in the sample measurements, the lids were analyzed in the laboratory to confirm that they were near zero percent reflectance and "spectrally flat" in the spectral range of the HSI instrument (1300 to 850 cm^{-1}); this is shown in Fig. 2(b) and confirms that there was minimal reflected light from the holders (lids) in the composite signal and that the longwave emitted light from the holders was relatively featureless. During the experiment, the polyethylene lids were filled with just enough powdered sample

Table 1 Typical experimental parameters for Bruker Tensor 37 solids reference measurements.

Parameter	Setting	Parameter	Setting
Infrared source	Glow bar	Phase resolution	32.0 cm^{-1}
Beamsplitter	KBr	Phase correction mode	Mertz/no pk search
Detector	LN_2 cooled MCT 2×2 mm	Apodization mode	Blackman Harris 3-term
Sampling acc.	A562 integrating sphere	Zerofilling factor	4
Mirror velocity	40 kHz	Co-added scans	2048 (typical)
Aperture	6 mm	High frequency limit	15,802.4 cm^{-1}
Laser frequency	15,802.4 cm^{-1}	Low frequency limit	0.0 cm^{-1}
Wavenumber range	7500 to 600 cm^{-1}	Low pass filter	40.0 kHz
Spectral resolution	4.0 cm^{-1}	High pass filter	Open
Acquisition mode	Dbl-sided forward backward	Switch gain	On – factor 8×

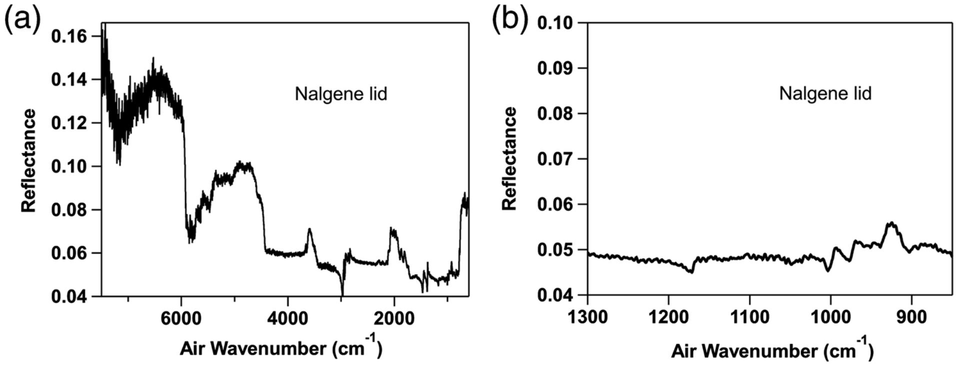

Fig. 2 Measured laboratory reflectance spectra of polyethylene (Nalgene) lid in the (a) 7500 to 600 cm^{-1} and (b) 1300 to 850 cm^{-1} spectral ranges.

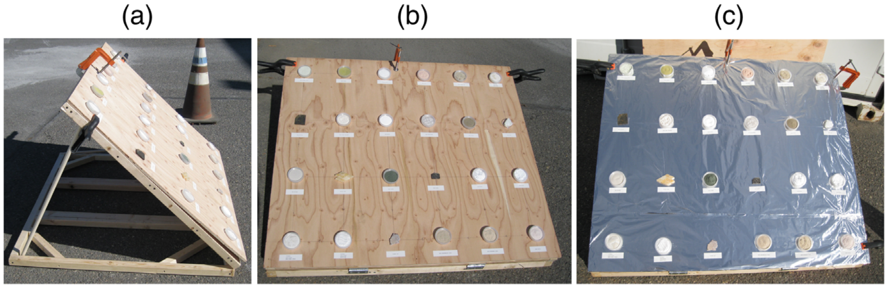

Fig. 3 Images of (a) frame (b) bare plywood board and (c) aluminum-foil coated board that were used in the experiment. Spring clamps secured the boards to the frame.

to avoid spillage at the 45-deg angle, though on a few occasions there was minimal spillage of some of the looser powders.

As shown in Fig. 3, the samples were regularly spaced with 8 in. between the columns and 11.3 in. between the rows on the plywood. The samples used for the HSI experiment were chosen to constitute a varied selection of spectral features, particle sizes, and sample forms. These included silica (SiO_2), bauxite $[Al(OH)_3]$, simple aluminosilicates (microcline and pyrophyllite), sheet aluminosilicates with additional metals (muscovite and montmorillonite), and mixtures of minerals, presented as mass percentages, to obtain a diverse representation as summarized in Table 2. We should note that some of these samples are provided in the ASTER spectral database, which includes spectra for three particle size fractions for over 150 of its mineral samples.[20] Since not only the particle size but also the sample provenance or origin can lead to differences in DHR spectra,[49] we only used the reference spectra measured in this study.

Some of the materials were selected in part based on known spectra, a few of which contained a significant peak or peaks that could be easily recognized in the 1300 to 850 cm^{-1} spectral range, such as muscovite and pyrophyllite. Conversely, others were selected due to being spectrally "flat" with few prominent features in the Telops spectral range. Infrared spectra were recorded for all the samples and were later used as reference endmembers in the spectral database that contained 21 pure minerals, 3 mixtures, and the polyethylene reference.

The HSI experiment was conducted over a 2-day period, on October 4 and 5, 2017, at Pacific Northwest National Laboratory (PNNL) campus (46.319°N, 119.283°W). Measurements were made over the course of the first day, in local time, from 10:57 until 21:29 Pacific Daylight Time (PDT) as one of the parameters to be studied was the diurnal variation of the spectral response. As mentioned, the Telops instrument measured the radiance in the 7.7 to 11.8 μm (1300 to 850 cm^{-1}) spectral range. A spectral resolution of 4 cm^{-1} was used for all the measurements, and typically eight datacubes were averaged for each scan, with four scans then averaged to improve the signal-to-noise ratio. The Telops incorporates an MCT focal plane array of 320×256 pixels with an instantaneous field of view of 350 μrad/pixel with the standard optic. The frame was placed at a distance of 14 m (45 ft) from the center of frame to center of the Telops

Table 2 Chemicals, minerals, rocks, and materials used. Particle size distributions measured via optical microscopy.

Material	Formula	Grain size (μm) or form	Supplier/origin
Faux onyx-calcite	$CaCO_3$	Rock	Arizona tile
Silica sand (50 to 70 mesh)	SiO_2	341 ± 93	Sigma-Aldrich
Sodium carbonate	Na_2CO_3	579 ± 184	Sigma-Aldrich
Calcium carbonate	$CaCO_3$	59 ± 25	Sigma-Aldrich
Ammonium phosphate dibasic	$(NH_4)_2HPO_4$	446 ± 417	Sigma-Aldrich
Sodium phosphate dibasic	Na_2HPO_4	38 ± 28	Sigma-Aldrich
Polyethylene (lid)	$(C_2H_2)_n$	Solid	Nalgene
Artinite	$Mg_2(CO_3)(OH)_2 \bullet 3H_2O$	Rock	San Benito Co., California
Bauxite	$Al(OH)_3$, AlO(OH), FeOOH	16 ± 12	Ward Scientific
Dickite	$Al_2Si_2O_5(OH)_4$	24 ± 14	St. George, Utah
Microcline	$KAlSi_3O_8$	12 ± 9	Parry Sound, Ontario, Canada
Nontronite	$(CaO_{0.5}, Na)_{0.3}Fe^{3+}{}_2(Si, Al)_4O_{10}(OH)_2 \bullet nH_2O$	202 ± 98	Garfield, Washington
Saponite	$Ca_{0.25}(Mg, Fe)_3((Si, Al)_4O_{10})(OH)_2 \bullet 4(H_2O)$	Rock	Isle of Mull, Scotland
Sericite	Mainly muscovite	104 ± 112	Imperial Co., California
Muscovite	$KAl_2(AlSi_3O_{10})(F, OH)_2$	19 ± 22	Stoneham, Maine
Pyrophyllite	$Al_2Si_4O_{10}(OH)_2$	Rock	Mariposa Co., California
Ripidolite	$(Mg, Fe, Al)_6(Si, Al)_4O_{10}(OH)_8$	25 ± 20	El Dorado Co., California
Clinoptilolite	$(Na, K, Ca)_{2\text{-}3}Al_3(Al, Si)_2Si_{13}O_{36} \bullet 12H_2O$	16 ± 13	Hector, California
Montmorillonite	$(Na, Ca)_{0.33}(Al, Mg)_2(Si_4O_{10})(OH)_2 \bullet nH_2O$	14 ± 10	Wyoming
Quincy soil		215 ± 89	Quincy, Washington
Mica–Schist	Micas, talc, hornblende	Rock	Ft. Collins, Colorado
Vermiculite	$(Mg, Fe, Al)_3(Al, Si)_4O_{10})(OH)_2 \bullet 4H_2O$	20 ± 15	Transvaal, Africa
Mixture 1	50% Na_2CO_3, 25% microcline, 25% nontronite	Mixture	
Mixture 2	50% silica sand, 50% $CaCO_3$	Mixture	
Mixture 3	75% Na_2CO_3, 25% sericite	Mixture	

tripod; thus, the instrument imaged a $1.56\ \text{m} \times 1.25\ \text{m}$ patch in object space. In preparing for the field experiment, a variable-angle plywood frame was constructed to which different pieces of plywood could be readily attached; each piece of plywood (sample) board was mounted with 24 samples to form a configuration. Each board was clamped to the frame using spring clamps (Fig. 3), allowing for quick exchange between measurements. The frame to hold the sample

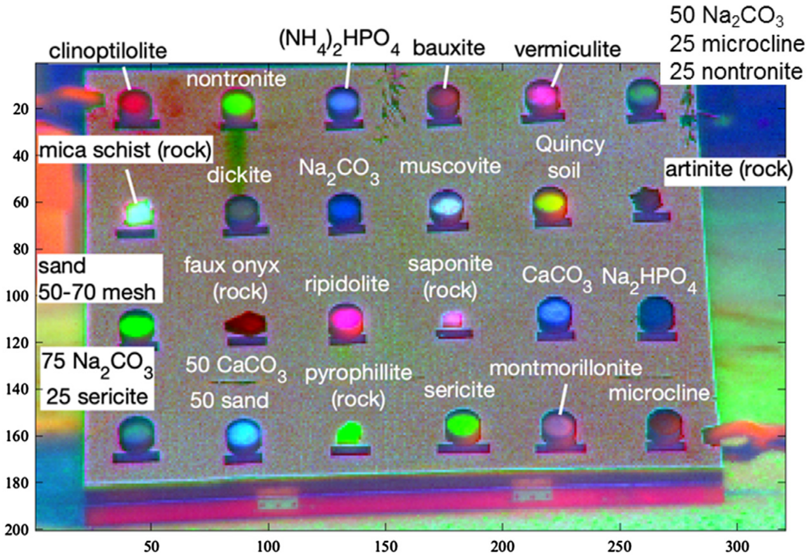

Fig. 4 RGB false color image of the scores on PCs 2, 3, and 4 for C1B145 (autocontrasted). The mineral and chemical materials are labeled, and the same configuration also holds for the other figures.

boards was constructed using stock lumber with the two frame boards each measuring 1.07 m × 1.22 m (42 × 48 in.) and hinged together at the front base as shown in Fig. 3. To achieve different tilt angles for the sample boards, wooden dowels were cut to different lengths and placed in the corners of the frame to achieve the desired angles for the experiment (25 deg, 35 deg, and 45 deg relative to the ground). The angles were verified using a protractor.

For two of the sample boards, 24 different minerals were attached to the frame—each mineral arrangement on a board was thus a "configuration." Of the 24 samples, 5 were in rock (single specimen) form taped directly to the board and the other 19 were displayed as powdered minerals (16 pure minerals and 3 mixtures). The powdered minerals were placed in the 2-in.-diameter polyethylene lids as described previously. Figure 4 shows the layout of the minerals for configuration 1, also shown in photos of Fig. 3. The position of the sample is referred to as [row #, column #]; for example, the position of sodium phosphate dibasic (Na_2HPO_4) is [3, 6]. Board 1 had the mineral samples mounted on plywood fully covered with reflective aluminum foil with the samples positioned as per Fig. 4. Board 3 was bare plywood but with the same minerals and configuration as board 1. (Board 2 included different samples and is not discussed in this paper.) The samples were swapped between the two boards using the same configuration, and each board was successfully staged at the three tilt angles (25 deg, 35 deg, and 45 deg), with (1) the Telops field of view (FOV) adjusted at each angle and (2) the HSI spectrometer recalibrated for each FOV. This procedure was repeated five times throughout the first day using different configurations. In this paper, only the results for the 45-deg orientation and configuration 1 are discussed.

3 Results

Analysis was performed for two boards: C1B145 and C1B345. C1B145 corresponded to configuration 1, board 1 (plywood coated with aluminum), 45 deg relative to ground, recorded on October 4, 2017, at 11:20 PDT, and C1B345 corresponded to configuration 1, board 3 (bare plywood), 45 deg tilt, recorded at 12:28 PDT. Image C1B345 was thus collected approximately an hour after C1B145, but both had the same configuration corresponding to the 24 mineral and rock samples mounted in a 4 × 6 pattern. Section 3.1 describes the results of an exploratory analysis of image C1B145 (i.e., with samples mounted on an aluminum foil background). Exploratory analysis was used to examine how the measured radiance signal manifests and if the minerals could be discriminated without extensive signal processing (i.e., no continuum removal was used for the exploratory analysis and spectra were not corrected for atmospheric interferences, most notably ozone $[O_3]$ and water vapor $[H_2O]$ in the 1250 to 1000 cm^{-1} domain, as discussed below). The analysis was also used, as described in Sec. 3.2, to select "representative blackbody and sky radiance" signal as inputs for the subsequent target detection.

Section 3.3 discusses results of target detection applied to the two concatenated images (C1B145 and C1B345). A simple radiance model is introduced and shows how target detection was employed using GLS applied to the processed signal. The signal was processed using the simple radiance model and manual selection of signal corresponding to blackbody and sky radiance, where the Telops measured the radiance of the (solar-heated) mineral samples. Although this signal processing can be considered rudimentary, it can be used to determine if simple processing can detect and discriminate mineral target signal in the image(s). Examples are shown using three representative targets: (1) ammonium phosphate dibasic, $(NH_4)_2HPO_4$; (2) calcium carbonate, $CaCO_3$; and (3) silica sand (50 to 70 mesh, i.e., 212 to 300 μm). The target detection results showed that discrimination was most successful for ammonium phosphate dibasic (due to its unique spectrum) and calcium carbonate (due primarily to its strong longwave reflectance). Detection results were poorest for artinite, sodium phosphate dibasic, clinoptilolite, sodium carbonate, and the poylethylene lid (all attributed to relatively low reflectance—the results are not shown). It is noted that detection was more successful when using the plywood background versus the aluminum background; this was attributed to the wood having an emissivity of ∼0.83 versus an emissivity of ∼0.04 for aluminum foil, i.e., the aluminum surface was reflecting sky radiance from colder atmospheric layers above.[31]

3.1 *Exploratory Analysis: Principal Component Analysis of Image C1B145*

PCA was used in an exploratory analysis of image C1B145. Spectra in the image were mean-centered prior to PCA decomposition, and the first principal component (PC 1) described >99% of the variance in the data and primarily captured the difference between the signal that resembles a graybody (Planck function) and the highly reflective aluminum background on board C1B145. Figure 5 shows that the loadings for PC 1 somewhat resemble a blackbody curve. The brightest samples on PC 1 (highest PCA scores on PC 1) were ripiodolite, vermiculite, and Quincy soil, which all have low-to-moderate reflectance values. Both ripidolite and vermiculite have measured infrared spectra that vaguely resemble a Planck blackbody function; this is discussed in detail below and is shown in Fig. 10(c); these curves display lower reflectance values, except for a single moderate reflectance peak in the 1040 to 1020 cm^{-1} domain. When radiance

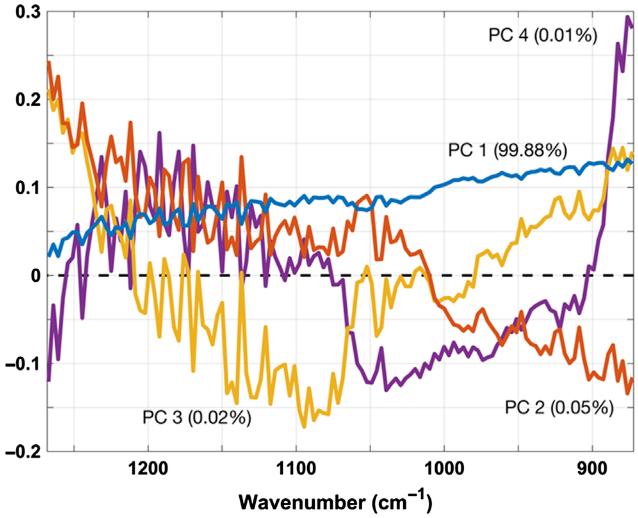

Fig. 5 PCA loadings on PCs 1 to 4 for C1B145. Much of the observed fine structure in the 1250 to 1100 cm^{-1} domain is due to atmospheric water lines. The PC loadings (PC 1 to PC 4) are the four principal components derived from reducing all the HSI experimental spectra to just the principal component as described in Sec. 3.1.

is converted to brightness temperature, the (brightness) temperature of the plywood mounting board C1B345 is very close to the ambient temperature of the surroundings, as expected. For the low emissivity aluminum-foil covered board C1B145, however, the sky is being reflected, which represents on average much cooler temperatures than the surroundings and is similar to the sky radiance.[31] Figure 4 shows an RGB false color image of the scores on PCs 2, 3, and 4 where the scores have been "autocontrasted" to enhance visualization, i.e., the scores have been mean-centered, scaled to a range of ±2 standard deviations, and saturated at values of ±2. This image is rich in information and shows clear detection and discrimination of the minerals. Rock samples (e.g., artinite) are easily recognized by their geometric shapes when compared with the round "dark-blue shadow" from the Nalgene sample cups that contain particulate or powdered mineral samples. Nalgene was chosen for its very low and flat spectral reflectance (Fig. 2), i.e., it has a significantly different flat signature than most of the powdered minerals and salts contained in the lids, causing the blue shadow. Sample labels are also visible on the mounting board as dark strips below each sample, indicating the configuration of the powders and rock minerals; the same relative configuration holds for all images in this paper.

The results shown in Figs. 4 and 5 are encouraging because they show that, using just four principal components and no further spectral processing or atmospheric compensation, the different materials are qualitatively easy to discriminate from each other, as well as from either the graybody background or highly reflective aluminum board. This suggests that the HSI signal can be used to detect and discriminate the mineral materials, but it is not yet clear if the target spectra in the database can be used to classify the materials. This will be discussed in the next section.

We note that the sharp spectral features seen in the PCA loadings 2 to 4 of Fig. 5 are due to the measured but weak "water vapor emission lines seen in the 1250 to 1150 cm^{-1} region," as noted by Farley et al.[50] primarily from atmospheric water vapor. Also observed are the branches of the ν_3 band of atmospheric ozone as seen in emission in the 1075 to 1000 cm^{-1} (9.6 μm) domain. As expected, emission lines due to water vapor are especially pronounced on the aluminum surface (where much of the background is reflected sky radiance) and are significantly represented in PCs 2 and 3. We note that these particular water ro-vibrational lines were apparently not included in some of the earlier versions of the high-resolution transmission molecular absorption database (HITRAN),[51] but they are included in the 2016 version of HITRAN.[52]

3.2 *Selection of Representative Blackbody and Sky Radiance Signal*

Representative values for the blackbody and sky radiance were estimated to provide a simple atmospheric correction to the data prior to target detection. The representative blackbody corresponded to the approximate maximum brightness temperature from a set of measured pixels that were closest to a blackbody response. In this case, PCA was performed with no signal processing to both boards, C1B145 and C1B345, which were augmented and analyzed simultaneously. Similar to the results in Fig. 5, PC 1 exhibited a near blackbody response and had a high score on the plywood, off-board background as well as the ripidolite mineral on the plywood board. Since PC1 manifested as approximately blackbody, the pixel with the maximum score on PC 1 was used to estimate the blackbody response from the Planck function at a temperature of 327 K.

The representative downwelling sky radiance was selected using PCA of the measured radiance processed using mean centered 1-norm normalized spectra. The procedure was similar to that for the blackbody signal except that preprocessing focused only on the highly reflective C1B145 board. Since PC 1 highlighted the highly reflective aluminum signal, the measured radiance from the pixel with the maximum score on PC 1 was used as representative sky radiance. Both the estimated blackbody and sky radiance from the scene are shown in Fig. 6.

3.3 *Target Detection: Generalized Least Squares for Augmented Images C1B145 and C1B345*

Target detection was based on a simple radiance model discussed below and was applied to boards C1B145 and C1B345, which were augmented and analyzed simultaneously for ease

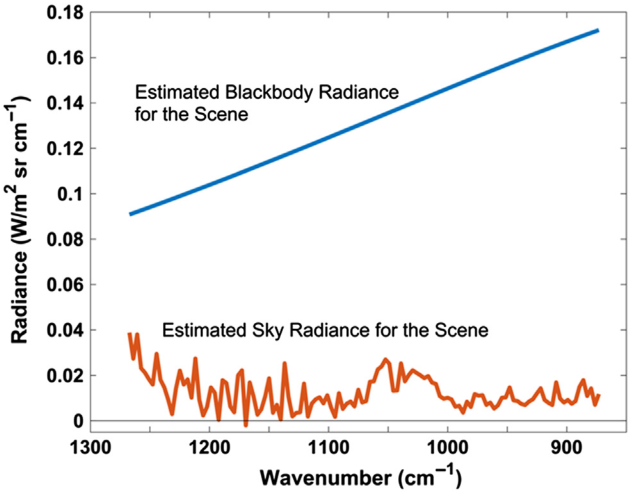

Fig. 6 The representative blackbody and sky radiance used for atmospheric correction.

of comparison of results. Several pixels in the scene corresponded to graybody signal and others corresponded to highly reflective low emissivity aluminum. Comparison of the two shows that while water emission lines in the sky radiance are clearly evident in the reflected spectra from aluminum (see PC loadings of Fig. 5), attenuation due to water vapor was not significant in the nonreflected graybody signal (not shown). This suggests that attenuation by water vapor, as the signal traverses the path between the target boards and the imaging spectrometer, was not significant, so attenuation due to the intervening atmosphere could be neglected in the simple radiance model. The result is a simple radiance model for the m'th pixel given as

$$x_m(v) = [1 - r_k(v)]b(T, v) + r_k(v)x_s(v), \tag{1}$$

where $x_m(v)$ is the measured radiance at frequency, v, r_k is the estimated reflectance for the k'th material, b is the Planck blackbody function at temperature T, and x_s is the sky-radiance incident on the scene. To keep the detection problem simple, it was assumed that the temperature and sky radiance across the scene were constant and "representative" values were selected from the exploratory analysis given in Sec. 3.2 and shown in Fig. 6. Thus, pixel-to-pixel variance in temperature and sky-radiance was neglected. For a pixel associated with a single material, the k'th material can be considered the k'th target of interest.

The hyperspectral image was measured over N frequencies that can be collected into an $N \times 1$ vector, $\mathbf{x}_m$, allowing Eq. (1) to be written as

$$\mathbf{x}_m = (\mathbf{1} - \mathbf{r}_k) \circ \mathbf{b} + \mathbf{r}_k \circ \mathbf{x}_s, \tag{2}$$

where $\circ$ is the element-by-element Hadamard product. Recall that $\mathbf{b}$ and $\mathbf{x}_s$ shown in Fig. 6 are assumed constant across the image. The simple radiance model given in Eq. (2) can be rearranged to isolate the measured reflectance in a pixel to yield

$$\mathbf{z}_m = (\mathbf{b} - \mathbf{x}_m) \circ/ (\mathbf{b} - \mathbf{x}_s) = c_{m,k}\mathbf{r}_k + \mathbf{e}_m, \tag{3}$$

where $\circ/$ is the element-by-element Hadamard division (there is no standard operator symbol for this operation), $c_{m,k}$ is introduced to allow for changes in the contribution of an individual target k, and $\mathbf{e}_m$ is introduced to account for modeling error. (Note that $\mathbf{e}_m$ is both target and pixel dependent and has two extremes: for a pixel that perfectly matches the library target of interest, $\mathbf{e}_m = \mathbf{0}$, but for a pixel that does not fit the library target of interest, $\mathbf{e}_m = \mathbf{z}_m$.) The right-hand expression of Eq. (3) approximates the measured reflectance as a linear mixture model of pure component reflectance spectra.

Signal in a pixel is rarely due to the presence of a single target analyte, and one approach to account for mixed signal pixels is to use the GLS model (a.k.a., the matched filter and the Aitkin estimator).[53–59] In the following, the objective function is defined as the left-hand expression and the corresponding estimator is given in the right-hand expression:

$$O(c_{m,k}) = (\mathbf{z}_m - c_{m,k}\mathbf{r}_k)^{\mathrm{T}}\mathbf{W}_j(\mathbf{z}_m - c_{m,k}\mathbf{r}_k) \rightarrow \hat{c}_{m,k} = (\mathbf{r}_k^{\mathrm{T}}\mathbf{W}_j^{-1}\mathbf{r}_k)^{-1}\mathbf{r}_k^{\mathrm{T}}\mathbf{W}_j^{-1}\mathbf{z}_m. \tag{4}$$

An important attribute of GLS is the use of the weighting (a.k.a., whitening) matrix $\mathbf{W}_j$, which was implemented in this work iteratively under the assumption that the target signal in the image is small relative to other sources of signal. In the context of signal processing, $\mathbf{W}_j$ is often called the clutter covariance.[60] For the augmented images, there were a total of M pixels and only the M_j "on-board" pixels were examined, where $M_j < M$ ("off-board" pixels were ignored). Therefore, the clutter covariance is estimated from

$$\mathbf{W}_j = \frac{1}{M_j}\mathbf{Z}_j^{\mathrm{T}}\mathbf{Z}_j, \tag{5}$$

where $\mathbf{Z}_j$ corresponds to the subset of M_j pixels and each row of $\mathbf{Z}_j$ is given by the expression in Eq. (3). It should be noted that mean-centering was not used in this estimate and that "covariance" should be read as "covariance about the origin."[58] For $j = 1$, M_j corresponded to all on-board pixels—including pixels potentially containing the target signal. In the second and final iteration ($j = 2$), pixels detected as the target were removed from $\mathbf{Z}_j$, resulting in a slightly more sensitive detection. Of course, iteration could continue, but two iterations sufficed to demonstrate the feasibility and characteristics of the detection strategy. Detections were determined using the following F-test at the 99% confidence limit:

$$\begin{gathered} f_{m,k} = (sse_{m,k,1} - sse_{m,k,2}) \Big/ \left(\frac{1}{M_j} sse_{m,k,2}\right) \\ sse_{m,k,1} = \mathbf{z}_m^{\mathrm{T}}\mathbf{W}_j^{-1}\mathbf{z}_m; \quad sse_{m,k,2} = (\mathbf{z}_m - c_{m,k}\mathbf{r}_k)^{\mathrm{T}}\mathbf{W}_j^{-1}(\mathbf{z}_m - c_{m,k}\mathbf{r}_k). \end{gathered} \tag{6}$$

Pixels with $f_{m,k} > f_{99\%}$ were considered detections. Detection images shown below are given a value of 0 for nondetections and are saturated at a high level of 2 (i.e., $f_{m,k} > 2f_{99\%}$ were set to a color value of 2).

For visualization, Fig. 7(a) shows PCA autocontrasted scores on PCs 3, 4, and 5 for images C1B145 (top, aluminum) and C1B345 (bottom, wood) augmented. No centering or scaling was used, and only on-board pixels were included in the PCA decomposition. The results are consistent with those seen for only C1B145 that used mean-centering (Sec. 3.1) and show that the minerals used for this study can be discriminated in a qualitative sense. Also, the color on the aluminum and plywood are similar for each mineral, indicating that the signal for the minerals was similar regardless of background material with only slight changes in the signal strength. Grain structure from the plywood is also evident in the lower image. The example targets are circled and labeled.

Figure 7(b) shows the target detection results for ammonium phosphate dibasic, $(\mathrm{NH}_4)_2\mathrm{HPO}_4$. The color-bar indicates the value of the F-statistic with dark blue corresponding to no detection and yellow corresponding to a strong detection. Because it is difficult to draw an exact one-to-one correlation between pixels and actual ground truth, conclusions are drawn by comparing Figs. 7(a) and 7(b). It is clear that $(\mathrm{NH}_4)_2\mathrm{HPO}_4$ was detected and correctly classified using target detection and that the detections appear somewhat stronger for the plywood mounting board (lower image). No apparent false positives were observed, as the ellipses corresponding to CaCO_3 and sand remain blue.

In a similar manner, Fig. 8(a) shows target detection results for the second target, namely calcium carbonate (CaCO_3). Figure 4 shows that pure CaCO_3 specimen is located at the [3,5] position on the mounting boards and that it is also present in a 50–50 mixture with silica sand at the [4,2] position. For the analysis, Fig. 8(a) shows that CaCO_3 was clearly detected and classified for the pure sample and in the 50–50 mixture for both the hyperspectral image on the plywood board and on the highly reflective Al board—no false positives are reported from the non-CaCO_3 samples. A comparison of the laboratory measured spectra for CaCO_3, sand 50–70 mesh, and the 50–50 mixture is given in Fig. 9 and clearly shows that CaCO_3 indeed has both a strong reflectance and a highly structured spectral signature. It also shows that the spectrum of the 50–50 mixture is quite similar to the pure CaCO_3 spectrum, thus indicating why CaCO_3 was easily detected in the mixture (although the quantitative reflectance is lower for the mixture).

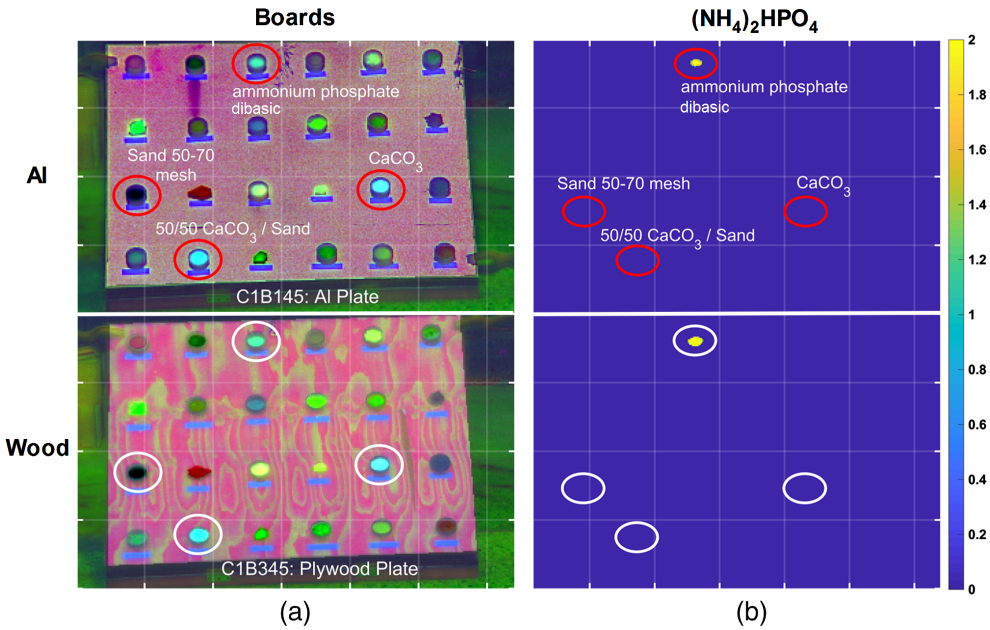

Fig. 7 (a) Scores image (autocontrasted) for visualization for images C1B145 (top) and C1B345 (bottom). (b) Target detection results for ammonium phosphate dibasic, $(NH_4)_2HPO_4$. Red and white ellipses circle example targets on the aluminum board and the plywood board, respectively. The detection for $(NH_4)_2HPO_4$ is indicated by yellow, whereas empty ellipses show "no detect" for the other targets.

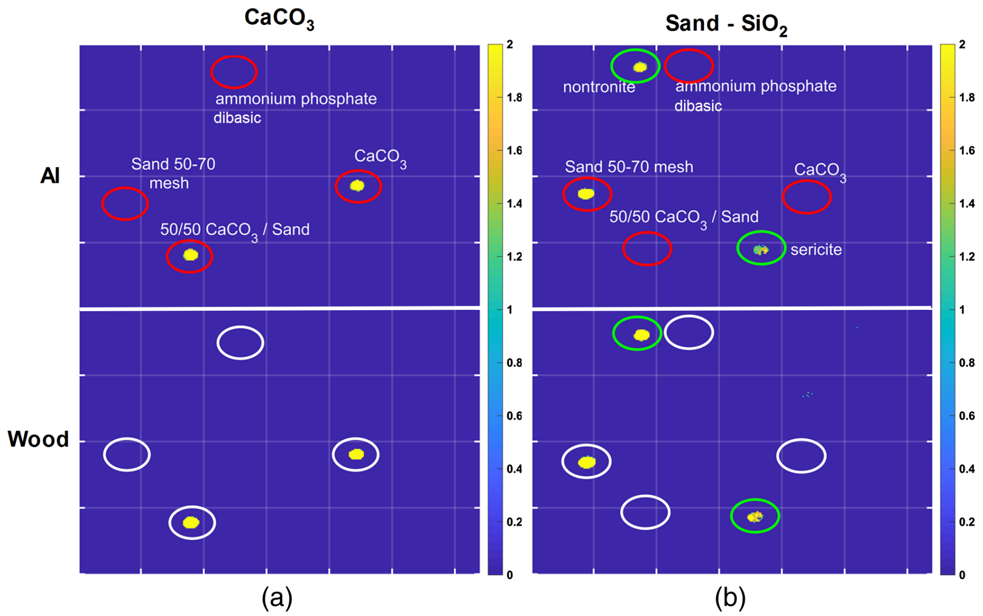

Fig. 8 (a) Target detection results for $CaCO_3$. The red and white ellipses (Al and plywood boards, respectively) identify locations of the example targets. (b) Target detection results for 50 to 70 mesh sand. Nominal "false positives" for nontronite/sericite are shown with green ellipses and discussed in text.

We also note that the fine $CaCO_3$ particles (59 ± 25 μm) and the coarser sand particles (341 ± 93 μm) were simply combined and shaken in a vial to provide the 50/50 mixture by mass. This preparation provided a mixture with a wide grain size distribution, and as discussed by Herzog and Mustard,[61] finer particles can dominate the reflectance spectrum, which may also partially explain why the spectrum of the 50–50 mixture more strongly resembles that of $CaCO_3$.

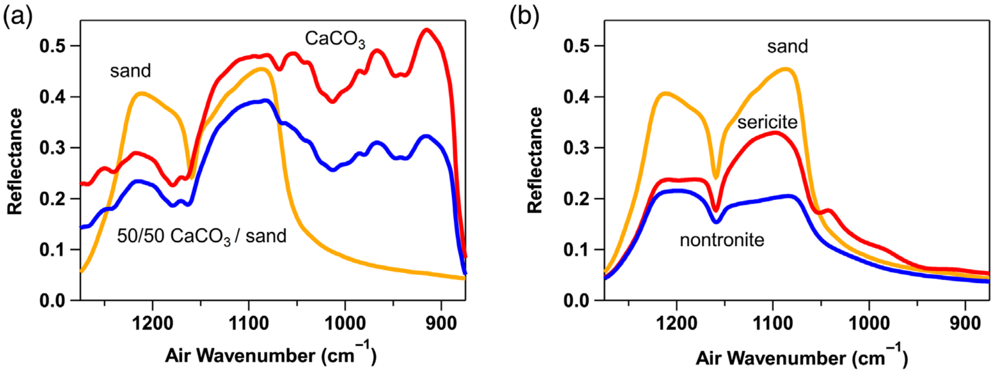

Fig. 9 (a) Measured laboratory reflectance spectra for calcium carbonate (red trace), 50 to 70 mesh sand (gold trace) and a 50%–50% mixture by mass of calcium carbonate and sand (blue trace). (b) Measured laboratory reflectance spectra for sand 50–70 mesh, sericite, and nontronite.

Figure 8(b) shows target detection results for sand (50–70 mesh). In this case, sand is clearly detected for the pure sample but is not found in the 50–50 mixture of $CaCO_3$ and sand. Comparison of the laboratory spectra [Fig. 9(a)] shows that the 50–50 mixture spectrum far more strongly resembles the signature of pure $CaCO_3$ than that of pure sand; the SiO_2 peaks from 1250 to 1050 cm^{-1} are largely masked by the stronger carbonate peaks, which may also result from the different particle sizes between $CaCO_3$ and sand in the mixture. Thus, it is not surprising that sand was not detected in the mixtures in the hyperspectral image. In addition to the true detection for the 50 to 70 mesh sand, Fig. 8(b) also shows apparent false positives for nontronite and sericite (circled in green). However, upon closer geochemical analysis, these detections are in fact not surprising; there is good reason for the sand/silica mixtures to be detected together, as seen by inspection of the spectra in Fig. 9(b). The SiO_2 features at 1085 and 1210 cm^{-1} are well known and are apparent in nearly all silicate spectra; the nontronite (Fe(III) rich smectite clay) and sericite (a fibrous variety of muscovite) minerals both have significant amounts of silicate giving rise to the similar spectral response. The chemical formula of nontronite is $Na_{0.3}Fe_2((Si,Al)_4O_{10})(OH)_2 \bullet nH_2O$, while sericite has the chemical formula $KAl_2(AlSi_3O_{10})(OH)_2$. As seen in the reference spectra in Fig. 9(b), nontronite and sericite both manifest as "low concentration" sand—the spectral peak positions are the same as those of silica—just with slightly reduced intensities. Thus, it makes physical sense that the silica and silicate minerals cluster together and generate "apparent" false positives. Interestingly, five pixels on Quincy soil (in the [2,5] position just above $CaCO_3$) and one pixel on the mixture at the [1,6] position (50% Na_2CO_3, 25% microline, and 25% nontronite) were also detected as false positive for sand on the plywood board. Comparison of the reflectance spectrum for Quincy soil compared with nontronite (not shown) confirms that, in a similar fashion, Quincy soil looks similar to "low concentration" nontronite, which explains the observed false positives.

4 Discussion

Analysis for both boards showed positive detection for ammonium phosphate dibasic, calcium carbonate, and silica/sand, although the silica signature was not detected in the sand sample physically mixed 50/50 with calcium carbonate. Although not shown, positive detections were also observed for pyrophyllite, mica-schist, and faux onyx-calcite. As expected, the spectra for targets with good detection or classification results tended to come from those minerals with the most structured reflectance spectra and larger percent reflectance (%R) values [Fig. 10(a)]. With moderate reflectance values, positive detections were observed for saponite, vermiculite, and ripidolite, but with false positives on each other. Figure 10(c) shows that this detection behavior is to be expected given the similarity of the spectra for these three minerals; all three are phyllosilicates with a moderately strong (14 to 20%R) reflectance peak centered around 1020 cm^{-1} (9.8 μm).

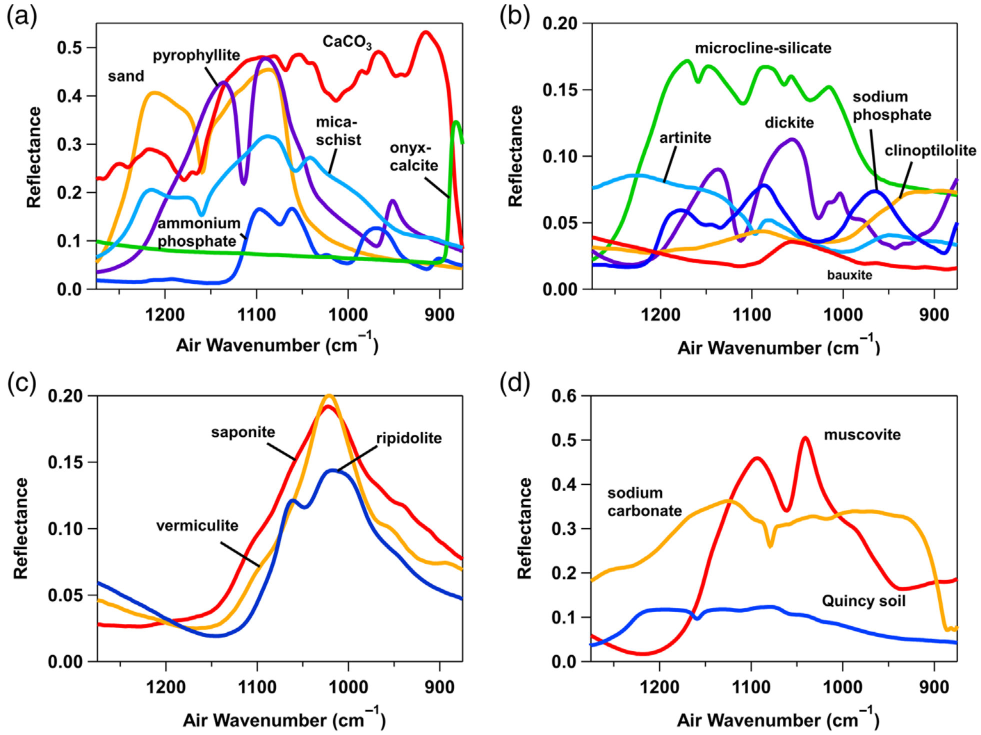

Fig. 10 Measured laboratory reflectance spectra. (a) Spectra for targets with good detection and classification: ammonium phosphate dibasic, calcium carbonate, sand, pyrophyllite, mica-schist, and faux onyx-calcite. (b) Spectra for targets with poor detection: artinite, bauxite, clinoptilolite, dickite, microline-silicate, and sodium phosphate dibasic. (c) "Graybody-like" spectra: saponite, vermiculite, and ripidolite. (d) Additional example spectra: Quincy soil, sodium carbonate, and muscovite. Note the different ordinate scales for the four plots.

The above results demonstrate the applicability of the laboratory DHR measurements for use in detection and classification of hyperspectral images of minerals. However, some targets are clearly more difficult to detect than others. For example, artinite, clinoptilolite, microline-silicate, sodium phosphate dibasic, and the polyethylene lid all had false negatives in this study [Fig. 10(b)]. This set of targets all had low to moderate reflectance values and cluster together (blue lines) in the *K*-means clustering dendrogram[60] shown in Fig. 11. Extending the spectral region to the VNIR or other IR regions may prove useful for successful detection of such species.[21] It is interesting to note that the low reflectance Quincy soil target had positive detections (with a few false positives on the plywood board for nontronite and the 50% Na_2CO_3, 25% microline, and 25% nontronite mixture), while sodium carbonate with high reflectance showed false negatives [Fig. 10(d)]. Muscovite had a similarly high reflectance as sodium carbonate but had positive detections (with false positives on saponite). The lack of positive detections for sodium carbonate is attributed to minimal structure in its processed spectral signature [e.g., Eq. (3), Fig. 10(d)] compared with muscovite that has a strong doublet feature near 1050 cm^{-1}.

The mixtures yielded varied results most likely due to the choice of minerals in the mixtures. In addition, the different particle sizes could lead to finer particles dominating the reflectance spectra since the minerals were simply mixed together. Best results were achieved for the 50% $CaCO_3$, 50% sand mixture in which the results for $CaCO_3$ showed positive detection for the 50/50 mixture although sand, which consisted of coarser grain sizes, was not detected in the 50/50 mixture. By contrast, both the 50% Na_2CO_3, 25% microcline-silicate, 25% nontronite mixture and the 75% Na_2CO_3, 25% sericite mixture showed false positives on sodium carbonate. This result, however, is not surprising since sodium carbonate was not observed with target detection due to its lack of spectral structure in the relevant spectral region [Fig. 10(d)]. Analysis on nontronite, however, did yield positive detection for some of the pixels on the high-emissivity plywood board with the 25% nontronite mixture but not with the low-emissivity,

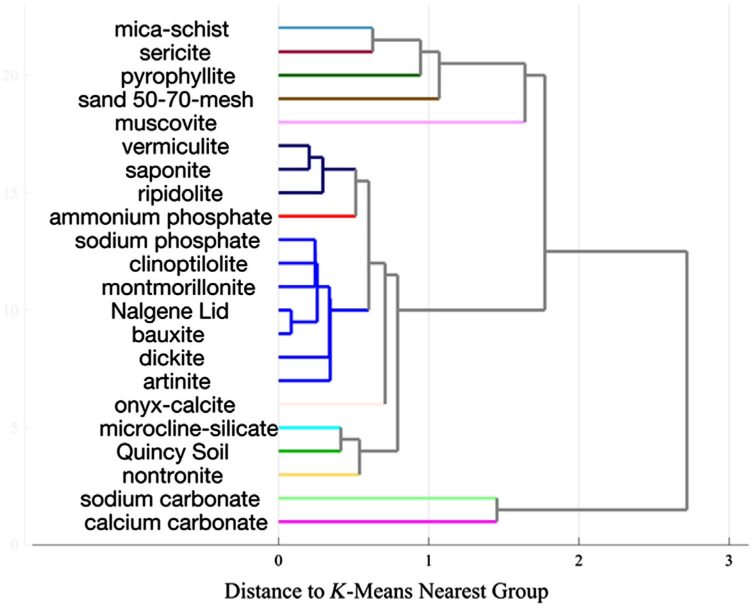

Fig. 11 *K*-means clustering dendrogram analysis results for the reflectance spectra for 21 different minerals and the Nalgene lid. The threshold for using different colors was set at 0.464.

aluminum-covered board. Neither microcline-silicate nor sericite yielded positive detection for the mixtures that had either 25% microcline-silicate or 25% sericite, respectively. This is to be expected for microcline-silicate since it was difficult to detect due to its low to moderate reflectance values [Fig. 10(b)]. Although sericite was clearly detected as the target, it was not detected in the 75/25 mixture even though it has a finer particle size distribution (104 ± 112 μm) than sodium carbonate (579 ± 184 μm).

Inspection of the dendrogram of Fig. 11 shows, not surprisingly, that many of the same mineralogical groups cluster together because of the similarity of their spectra: the carbonates (Na and Ca) form the most distinct cluster. Interestingly, though, sodium carbonate, unlike calcium carbonate, was not detected; the particle size distribution for $CaCO_3$ corresponded to finer particles (59 ± 25 μm) whereas sodium carbonate consisted of larger particles (579 ± 184 μm). As discussed by Myers et al.,[44] the smaller grain sizes generally lead to higher reflectance values due to volume scattering, except for the reststrahlen bands. The reststrahlen band for the carbonates, however, is around 1420 cm^{-1}, which is outside the spectral range used by the Telops sensor. Several of the silicates (pyrophyllite, sand, sericite, and mica-schist) form a cluster seen at the top of the dendrogram due to broad reflectance bands in the 1250 to 1050 cm^{-1} domain. As discussed, vermiculite, saponite, and ripidolite are all phyllosilicates and all have spectra similar to one another [Fig. 10(c)] with a moderate peak near 1020 cm^{-1}; these form the second cluster (navy blue) near the top of the dendrogram.

Observations from this study suggest that targets with both high reflectance and articulated spectral structure in the 7.7- to 11.8-μm spectral region of the Telops are the easiest to detect and classify. However, this study considered only a single simple signal processing and did not optimize the spectral processing for detection of different spectral forms as this was outside the present scope. Moreover, no attempt was made to optimize detection thresholds (e.g., 99% confidence limit for the *F*-test was used). As expected, it was also observed that mixtures were somewhat difficult to detect and classify using the single target detection algorithm.

Results from PCA in Sec. 3.1 displayed clear visual evidence that the minerals could be discriminated and were consistent with results shown in Sec. 3.3. This is important for two reasons. First, no significant signal processing or atmospheric compensation was used before PCA decomposition. The second reason is that a simple atmospheric correction followed by target detection was shown to be useful in Sec. 3.3, suggesting that this method may offer a rapid survey mode to identify images that require additional processing. This simple model, however, required some knowledge of the scenario and reflectance in the scene (e.g., the aluminum board was used to estimate the downwelling sky radiance). The model also assumed the same sky-radiance and the same temperature across the image and neglected attenuation of the atmosphere between the target scene and the sensing spectrometer. It is anticipated that improvements over these assumptions could improve the detection and classification performance. Unfortunately, radiance modeling may still present limits to fully realizing the potential of target-based algorithms. Target detection yielded false negatives for artinite, while the scores image shown in Fig. 4 clearly showed that artinite had a signal different from other minerals. It has been shown that combining target and anomaly detection approaches (e.g., PCA can be considered an anomaly detection approach) allows for empirically enabling target detection to be more sensitive and more relevant to image specific scenarios.[62] Thus, "targeted anomaly detection" synergistically employs laboratory measured spectra with empirical detection methods to provide an approach optimized for individual scenarios and will be investigated in future studies.

As discussed above, the PCA analysis quickly recognized that some of the brightest samples (i.e., least reflective) had measured infrared spectra that most looked like a Planck function with only one moderate band, e.g., ripidolite and vermiculite. This was shown in Fig. 10(c); the samples all display low reflectance values, with a modest peak near $\sim 1020\ \mathrm{cm}^{-1}$. While other species in this study have similar spectral profiles, namely low reflectance, some of these materials have distinct spectral features that can be used for identification. In fact, the $(\mathrm{NH}_4)_2\mathrm{HPO}_4$ spectrum displays some distinct features that can be used for identification, namely the $\mathrm{NH}_4{}^+$ cation peak at $970\ \mathrm{cm}^{-1}$, as well as the 1060, $1100\ \mathrm{cm}^{-1}$ doublet that we have previously associated as being two of the phosphate anion band modes.[27]

As to the strong reflectance peaks associated with symmetric cations[46,63–65] such as $\mathrm{NH}_4{}^+$ or $\mathrm{UO}_2{}^{2+}$ as well as anions[27,44] such as $\mathrm{PO}_4{}^{3-}$ or $\mathrm{SO}_4{}^{2-}$, these peaks arise from the first surface scattering of reststrahlen bands. As we have previously reported in studies that quantified reflection versus wavelength as a function of particle size,[44] the amplitude of the other bands relative to the reststrahlen bands varies significantly with particle size. It was shown that the various spectral phenomena (reststrahlen bands, Christensen minima, volume scattering, and transparency bands) could largely be understood by particle size in combination with the relative amplitudes of n and k, the real and imaginary components of the refractive index, respectively. For these reasons, it is recommended to construct solids spectral databases that either (a) include different particle sizes (e.g., the ASTER data set)[20] or (b) have methods to generate the spectral response for different particle sizes starting only with the n/k values and a few morphological parameters. This is especially true as we have extended the use of laboratory reflectance data for detection to infrared wavelengths where morphological effects can cause great spectral variation in the IR, especially for mixtures and for mixed particle sizes. Such particle size and morphological effects are far less pronounced for studies at visible or near-infrared wavelengths.[66] The infrared studies reported here all used the same physical samples for the HSI experiment as were used for the laboratory DHR reference data, so it was not necessary to account for such morphological factors; in most HSI experiments, this is not the case.

5 Conclusions

The present experiment has shown that a spectral database of minerals, mineral powders, and related solids that were recorded as DHR data in the laboratory can be readily deployed for HSI field detection in the LWIR. By constructing a synthetic mosaic of different minerals and mounting them on a target board, we were able to simulate LWIR detection of different minerals in the field or natural environment including both in rock and powdered forms, similar to other studies in the visible and near-infrared.[67] The reference library consisted of strictly laboratory DHR end-member spectra of 21 pure minerals, 3 mixtures, and the Nalgene reference. Using relatively simple methods, we demonstrated good detection and classification for ammonium phosphate dibasic, calcium carbonate, and silica sand, although the silica was not detected in the silica/calcium carbonate (50/50) mixture. PCA showed that the majority of the signal in the measured images could be attributed to differences between the signal from nonreflective blackbody signal and highly reflective aluminum surfaces. This result is consistent with the interpretation of the simple radiance model used here [Eq. (1)]. It was encouraging to note that a minor signal associated with other principal components clearly showed qualitative (visual) discrimination of the target minerals and that target detection using laboratory measured spectra could detect and discriminate several minerals using a fairly simple signal processing coupled with target detection. These results demonstrate the feasibility of mineral detection and classification using a portable HSI spectrometer and simple algorithms for a rapid, exploitation approach to indicate which cubes might need further processing. It is anticipated that better results can be obtained with more sophisticated algorithms[39,68,69] such as the moderate resolution atmospheric transmission (MODTRAN) module,[68] that adequately account for the effects of the atmosphere including its radiance, absorption by water vapor and other absorbers, aerosols, solar angle, etc. These methods are actively being explored.

Acknowledgments

This work was partly supported by the U.S. Department of Energy, National Nuclear Security Administration, Office of Defense Nuclear Nonproliferation (DNN, NA-22). We thank our sponsor for their support. The Pacific Northwest National Laboratory is operated for the United States Department of Energy by the Battelle Memorial Institute under contract DE-AC05-76RLO 1830. The authors declare that there is no conflict of interest.

References

1. M. E. Schaepman et al., "Earth system science related imaging spectroscopy: an assessment," *Remote Sens. Environ.* **113**, S123–S137 (2009).
2. G. Asrar, Ed., *Theory and Applications of Optical Remote Sensing*, John Wiley and Sons, Inc., New York (1989).
3. A. F. H. Goetz, "Three decades of hyperspectral remote sensing of the Earth: a personal view," *Remote Sens. Environ.* **113**, S5–S16 (2009).
4. T. J. Johnson et al., "An infrared spectral database for detection of gases emitted by biomass burning," *Vib. Spectrosc.* **53**, 97–102 (2010).
5. R. Lindenmaier et al., "Quantitative infrared absorption spectra and vibrational assignments of crotonaldehyde and methyl vinyl ketone using gas-phase infrared, far-infrared and liquid raman spectra: s-cis v. s-trans composition confirmed via temperature studies and ab initio methods," *J. Phys. Chem. A* **121**, 1195–1212 (2017).
6. J. M. Theriault, E. Puckrin, and H. Lavoie, "Remote monitoring of multi-gas mixtures by passive standoff Fourier transform infrared radiometry," *Appl. Spectrosc.* **61**(6), 630–637 (2007).
7. M. J. Mattu et al., "Quantitative analysis of sulfur dioxide with passive Fourier transform infrared remote sensing interferogram data," *Appl. Spectrosc.* **54**(3), 341–348 (2000).
8. H. J. Mitchell and C. Salvaggio, "MWIR and LWIR spectral signatures of water and associated materials," *Proc. SPIE* **5093**, 195–205 (2003).
9. M. Masse et al., "Spectroscopy and detectability of liquid brines on Mars," *Planet. Space Sci.* **92**, 136–149 (2014).
10. B. E. Bernacki et al., "Modeling liquid organic thin films on substrates," *Proc. SPIE* **10629**, 1062916 (2018).
11. F. A. Kruse, J. W. Boardman, and J. F. Huntington, "Comparison of airborne hyperspectral data and EO-1 Hyperion for mineral mapping," *IEEE Trans. Geosci. Remote Sens.* **41**(6), 1388–1400 (2003).
12. B. E. Bernacki et al., "Visible hyperspectral imaging for standoff detection of explosives on surfaces," *Proc. SPIE* **7838**, 78380C (2010).
13. N. Pasqualotto et al., "Retrieval of canopy water content of different crop types with two new hyperspectral indices: water absorption area index and depth water index," *Int. J. Appl. Earth Obs. Geoinf.* **67**, 69–78 (2018).
14. B. Ribeiro da Luz and J. K. Crowley, "Spectral reflectance and emissivity features of broad leaf plants: Prospects for remote sensing in the thermal infrared ($8.0 - 14.0\ \mu$m)," *Remote Sens. Environ.* **109**, 393–405 (2007).

15. G. P. Asner et al., "Spectroscopy of canopy chemicals in humid tropical forests," *Remote Sens. Environ.* **115**, 3587–3598 (2011).
16. B. L. Cooper et al., "Mid-infrared spectral features of rocks and their powders," *J. Geophys. Res.* **107** (E4), 5017 (2002).
17. G. R. Hunt and J. W. Salisbury, "Mid-infrared spectral behavior of igneous rocks," *Environmental Research Paper*, U.S. Air Force, Cambridge Research Laboratory (1974).
18. G. R. Hunt and J. W. Salisbury, "Mid-infrared spectral behavior of sedimentary rocks," *Air Force Cambridge Research Laboratories Report*, Number AFCRL-ERP-520, pp. 1–48 (1975).
19. G. R. Hunt and J. W. Salisbury, "Mid-infrared spectral behavior of metamorphic rocks," *Environmental Research Paper*, U.S. Air Force, Cambridge Research Laboratory (1976).
20. A. M. Baldridge et al., "The Aster spectral library version 2.0," *Remote Sens. Environ.* **113**, 711–715 (2009).
21. F. D. van der Meer et al., "Multi- and hyperspectral geological remote sensing: a review," *Int. J. Appl. Earth Obs. Geoinf.* **14**(1), 112–128 (2012).
22. A. B. Kahle et al., "The advanced spaceborne thermal emission and reflectance radiometer (ASTER)," *Int. J. Imaging Syst. Technol.* **3**(2), 144–156 (1991).
23. J. E. Conel, "Infrared emissivities of silicates: experimental results and a cloudy atmosphere model of spectral emission from condensed particulate mediums," *J. Geophys. Res.* **74**, 1614–1634 (1969).
24. M. D. Lane, "Mid-infrared optical constants of calcite and their relationship to particle size effects in thermal emission spectra of granular calcite," *J. Geophys. Res.* **104** (E6), 14099–14108 (1999).
25. V. E. Hamilton, "Thermal infrared (vibrational) spectroscopy of Mg-Fe olivines: a review and applications to determining the composition of planetary surfaces," *Geochemistry* **70** (1), 7–33 (2010).
26. F. E. Volz, "Infrared optical constants of ammonium sulfate, Sahara dust, volcanic pumice, and flyash," *Appl. Opt.* **12**(3), 564–568 (1973).
27. T. N. Beiswenger et al., "Identification of uranium minerals in natural U-bearing rocks via infrared reflectance spectroscopy," *Appl. Spectrosc.* **72** (2), 209–224 (2017).
28. B. M. DeVetter et al., "Optical and chemical characterization of uranium dioxide (UO_2) and uraninite mineral: calculation of the fundamental optical constants," *J. Phys. Chem. A* **122**, 7062–7070 (2018).
29. A. Rein and F. Higgins, "Hand-held FTIR analyzers: a new capability for at-Site measurements of rock and minerals– use of FTIR for elucidating rock and mineral composition," *Spectroscopy* **18**, 16–17 (2010).
30. G. C. Davenport, "Remote sensing applications in forensic investigations," *Hist. Archaeol.* **35**(1), 87–100 (2001).
31. T. A. Blake et al., "Passive standoff detection of RDX residues on metal surfaces via infrared hyperspectral imaging," *Anal. Bioanal. Chem.* **395**, 337–348 (2009).
32. P. Lagueux et al., "Airborne infrared hyperspectral imager for intelligence, surveillance and reconnaissance applications," *Proc. SPIE* **8542**, 836004 (2012).
33. P. G. Lucey et al., "Three years of operation of AHI: the University of Hawaii's Airborne Hyperspectral Imager," *Proc. SPIE* **4369**, 112–120 (2001).
34. J. A. Hackwell et al., "LWIR/MWIR imaging hyperspectral sensor for airborne and ground-based remote sensing," *Proc. SPIE* **2819**, 102–107 (1996).
35. D. W. Warren et al., "MAKO: a high-performance, airborne imaging spectrometer for the long-wave infrared," *Proc. SPIE* **7812**, 78120N (2010).
36. W. R. Johnson, G. Hulley, and S. J. Hook, "Remote gas plume and imaging with NASA's hyperspectral thermal emission spectrometer (HyTES)," *Proc. SPIE* **9101**, 91010V (2014).
37. Z. Aslett, J. V. Taranik, and D. N. Riley, "Mapping rock forming minerals at Boundary Canyon, Death Valley National Park, California, using Aerial SEBASS thermal infrared hyperspectral image data," *Int. J. Appl. Earth Obs. Geoinf.* **64**, 326–339 (2018).
38. T. L. Myers et al., "The influence of particle size on infrared reflectance spectra," *Proc. SPIE* **9088**, 908809 (2014).

39. J. Theiler et al., "Spectral variability of remotely sensed target materials," *IEEE Geosci. Remote Sens. Mag.* **7**(2), 8–30 (2019).
40. T. J. Johnson, T. Masiello, and S. W. Sharpe, "The quantitative infrared and NIR spectrum of CH_2I_2 vapor: vibrational assignments and potential for atmospheric monitoring," *Atmos. Chem. Phys.* **6**, 2581–2591 (2006).
41. L. T. M. Profeta et al., "Quantitative infrared intensity studies of vapor-phase glyoxal, methylglyoxal, and 2, 3-butanedione (diacetyl) with vibrational assignments," *J. Phys. Chem. A* **115**, 9886–9900 (2011).
42. A. Le Bras and S. Erard, "Reflectance spectra of regolith analogs in the mid-infrared: effects of grain size," *Planet Space Sci.* **51** (4), 281–294 (2003).
43. G. R. Hunt and L. M. Logan, "Variation of single particle mid-infrared emission spectrum with particle size," *Appl. Opt.* **11** (1), 142–147 (1972).
44. T. L. Myers et al., "Quantitative reflectance spectra of solid powders as a function of particle size," *Appl. Opt.* **54** (15), 4863–4875 (2015).
45. T. A. Blake et al., "Methods for quantitative infrared directional-hemispherical and diffuse reflectance measurements using an FTIR and a commercial integrating sphere," *Appl. Opt.* **57**(3), 432–446 (2018).
46. T. J. Johnson et al., "Time-resolved infrared reflectance studies of the dehydration-induced transformation of uranyl nitrate hexahydrate to the trihydrate form," *J. Phys. Chem. A* **119**, 9996–10006 (2015).
47. A. J. Rettie et al., "Synthesis, electronic transport and optical properties of Si: α-Fe_2O_3 single crystals," *J. Mat. Chem. C.* **4** (3), 559–567 (2016).
48. M. Koehl and K. Forcht, "The experimental assessment of the effects of non-Lambertian surfaces on integrating sphere measurements in the mid-IR," *Proc. SPIE* **5192**, 61–68 (2003).
49. Y. F. Su et al., "Infrared reflectance spectra: effects of particle size, provenance and preparation," *Proc. SPIE* **9253**, 925304, (2014).
50. V. Farley et al., "Radiometric calibration stability of the FIRST: a longwave infrared hyperspectral imaging sensor," *Proc. SPIE* **6206**, 62062A (2006).
51. L. S. Rothman et al., "The HITRAN molecular spectroscopic database and HAWKS (HITRAN Atmospheric Workstation): 1996 edition," *J. Quant. Spectrosc. Radiat. Transfer* **60**, 665–710 (1998).
52. I. E. Gordon et al., "The HITRAN2016 molecular spectroscopic database," *J. Quant. Spectrosc. Radiat. Transfer* **203**, 3–69 (2017).
53. A. Aitken, "On least squares and linear combinations of observations," *Proc. R. Soc. Edinburgh* **55**, 42–48 (1935).
54. C. C. Funk et al., "Clustering to improve matched filter detection of weak gas plumes in hyperspectral imagery," *IEEE Trans. Geosci. Remote Sens.* **39**(7), 1410–1420 (2001).
55. J. R. Magnus and H. Neudecker, *Matrix Differential Calculus with Applications in Statistics and Economics*, John Wiley & Sons, New York (1999).
56. H. Martens and T. Næs, *Multivariate Calibration*, John Wiley & Sons, Ltd., New York (1989).
57. N. B. Gallagher, "Detection, classification and quantification in hyperspectral images using classical least squares models," in *Techniques and Applications of Hyperspectral Image Analysis*, H. F. Grahn and P. Geladi, Eds., pp. 181–201, John Wiley & Sons, West Sussex, England (2007).
58. N. B. Gallagher, "Classical least squares for detection and classification," in *Hyperspectral Imaging*, Data Handling in Science and Technology, 1st ed., J. Manuel Amigo, Ed., Vol. **32**, Elsevier, Oxford (2019).
59. T. Burr and N. Hengartner, "Overview of physical models and statistical approaches for weak gaseous plume detection using passive infrared hyperspectral imagery," *Sensors* **6**, 1721–1750 (2006).
60. K. V. Mardia, J. T. Kent, and J. M. Bibby, *Multivariate Analysis*, Academic Press, Amsterdam (1979).
61. S. G. Herzog and J. F. Mustard, "Reflectance spectra of five-component mineral mixtures: Implications for mixture modeling," *Lunar Planet. Sci.* **27**, 535–536 (1996).

62. N. B. Gallagher et al., "Decompositions with maximum signal factors," *J. Chemom.* **28**(8), 663–671 (2014).
63. E. Faulques et al., "Spectroscopic markers for uranium (VI) phosphates: a vibronic study," *RSC Adv.* **5**(87), 71219–71227 (2015).
64. N. Kalashnyk et al., "Exploring optical and vibrational properties of the uranium carbonate andersonite with spectroscopy and first-principles calculations," *J. Phys. Chem. C* **122**(13), 7410–7420 (2018).
65. M. C. Kirkegaard et al., "Vibrational properties of anhydrous and partially hydrated uranyl fluoride," *J. Chem. Phys.* **146**, 024502 (2017).
66. T. J. Johnson et al., "Intensity-value corrections for integrating sphere measurements of solid samples measured behind glass," *Appl. Spectrosc.* **68**(11), 1224–1234 (2014).
67. R. A. V. Rossel et al., "Visible, near infrared, mid infrared or combined diffuse reflectance spectroscopy for simultaneous assessment of various soil properties," *Geoderma* **131**(1–2), 59–75 (2006).
68. A. Berk et al., "MODTRAN6: a major upgrade of the MODTRAN radiative transfer code," *Proc. SPIE* **9088**, 90880H (2014).
69. L. S. Berstein et al., "Quick atmospheric correction code: algorithm description and recent upgrades," *Opt. Eng.* **51**(11), 111719 (2012).

Tanya L. Myers received her PhD in chemistry from the University of Chicago and her BS degree in chemistry from the University of North Carolina at Chapel Hill. She is currently a senior scientist at Pacific Northwest National Laboratory (PNNL). Before joining PNNL, she was the National Research Council postdoctoral fellow with NIST at JILA at the University of Colorado in Boulder. Her current research interests include quantitative measurement of optical constants for solids and liquids.

Timothy J. Johnson is a cum laude graduate of Carleton College and received his PhD in chemical physics from Washington State University in 1987. He is currently a senior scientist at PNNL and has extensive experience with spectroscopic signatures, including contributions to the PNNL gas-phase database and other high fidelity spectroscopic signature efforts including for solids and liquids. He has led efforts for better quantitation using visible and infrared reflectance, as well as Raman spectroscopy.

Neal B. Gallagher received his PhD in chemical engineering with a mathematics minor from the University of Arizona in 1992. He is vice president and cofounder of Eigenvector Research, Inc., where he specializes in chemometrics consulting, algorithm development for detection, classification and quantification, chemometrics research, short courses, and software.

Bruce E. Bernacki received his PhD in optical sciences from the University of Arizona. Prior to joining PNNL, he spent nearly 5 years as vice president of New Product Development and CTO at LightPath Technologies, in Orlando, Florida, USA. His experience includes optical design, modeling, optical data storage, and optical component manufacturing. He has received two R&D 100 awards for his inventions in 2014 and 2017.

Toya N. Beiswenger received her master's degree in environmental science from Washington State University and her BS degree in biology from Southeastern Louisiana University. She is a staff scientist at PNNL. Before joining PNNL, she was a forensic scientist at the St. Tammany Parish Sheriff's Office where she conducted analysis of gunshot residue. Her current research interests include applying analytical techniques such as spectroscopy, microscopy, and tomography to identifying signatures for various materials.

James E. Szecsody received his PhD in hydrology with a minor in geochemistry/soil science from the University of Arizona. He received his MS degree in hydrology/hydrogeology from the University of Nevada and his BS degree in geology from Arizona State University. He is a senior scientist at PNNL, and his research interests include developing and testing remediation technologies for chlorinated solvents, energetics, and radionuclides. He received an R&D 100 award in 1998.

Russell G. Tonkyn received his BA degree in chemistry from Reed College and his PhD in physical chemistry from the University of Wisconsin at Madison. Prior to joining PNNL, he had a postdoctoral position at Brookhaven National Laboratory. He has worked on many diverse projects over the years, including various gas, liquid, and solid databases using FTIR and Raman spectroscopy.

Ashley M. Bradley received her BS degree in biochemistry with a double major in genetics and cell biology along with a minor in molecular biology from Washington State University in 2016. She has worked at PNNL since 2017.

Yin-Fong Su recently retired from PNNL.

Tyler O. Danby received dual bachelor's degrees in biological science and general history from Washington State University in 2015. From 2016 to 2018, he worked at PNNL as a postbachelor research associate and contributed to several scientific projects during this time.